Growth and study of *c*-axis-oriented vertically aligned ZnO nanorods on seeded substrate

Anu Katiyar[1], Nishant Kumar[1,2], R. K. Shukla[1], and Anchal Srivastava[1,*]

[1] *Department of Physics, University of Lucknow, Lucknow 226007, U.P, India*
[2] *Department of Physics, School of Science, Maharishi University of Information Technology, Lucknow 226013, U.P, India*

ABSTRACT

ZnO nanorods (NRs) are grown by sonicated sol–gel immersion method at a lower temperature, along c-axis, i.e., normal to the glass substrate spin-coated with seed-layer of zinc oxide. Effects of seed-layer-precursor molarity and immersion time on the structural and morphological properties of NRs have been investigated. These two process parameters affect the diameter and length of the ZnO NRs significantly. The NRs are hexagonal in cross section. The polycrystalline seed-layer with nano-sized grains exhibits high transparency and quick photoresponse. The transmittance decreases after the growth of NRs but improves past annealing. The band gap value of bulk ZnO is tuned up to 190 meV by the growth of NRs and their subsequent annealing. These NRs exhibit green emission and persistent photoconductivity (PPC). The annealing of NRs quenches the green emission and reduces the PPC effect partially.

1 Introduction

Zinc oxide is a widely studied n-type II-VI compound semiconductor material with a wide band gap of 3.37 eV and a large exciton binding energy of 60 meV at room temperature. It is a stable, economic, and environment-friendly oxide material with a wide range of high technology applications as well as applications in everyday products. The wurtzite structured ZnO with two important characteristics noncentral symmetry and (0001) polar surface exhibits piezoelectric and pyroelectric properties as well as the highest growth rate along *c*-axis [1]. The unique anisotropic structure of wurtzite ZnO exhibits a diverse group of morphological nanostructures such as nanorods, nanowires, nanobelts, nanosprings, nanowhiskers, nanocombes, nanorings, nanocages, nanohelices, nanodisks. [1–3]. Nanostructured ZnO in the form of nanobelts, nanorods, nanowires, etc., shows better response as gas sensor as larger surface-to-volume ratio allows the greater exchange of charge carriers during oxidation/reduction mechanism [4]. The vertically aligned ZnO nanorods (NRs) have attracted much attention due to its high surface-to-volume ratio facilitating numerous novel applications including light-emitting diodes (LEDs), photodetectors, sensors, liquid crystal device (LCDs), and solar cell. Previously, successive ionic layer absorption and reaction (SILAR) technique has been used for both ZnO nanostructured thin film [5]

---

and ZnO seed layers [6, 7] growth. Kumar et al. [7] have used SILAR ZnO seed layer films for controlled growth of ZnO nanorods at different pH concentration via chemical bath deposition (CBD) method. Recently, George et al. [8] have used hydrothermal and solvothermal methods for the preparation of nickel vanadium oxide nanoparticles. Various methods of synthesis have been reported including chemical bath deposition (CBD), thermal evaporation, hydrothermal, sonicated sol–gel immersion, and chemical vapor deposition (CVD) [9–17]. Among these approaches, sonicated sol–gel immersion method is a simple and low-cost method, while facilitating large area coating, to prepare good quality and highly c-axis-oriented vertically aligned ZnO NRs at temperatures lower than 100°C. A variety of ZnO thin film-based seed-layers [18, 19] on a variety of substrates like FTO & ITO [9, 20–23], Si [12, 24–27], ITO-coated PET [28], and quartz [14] have been reported for the growth of ZnO NRs. ZnO thin film effectively reduces the nucleation energy barrier due to the lattice match between the thin film and NRs [2]. The growth of c-axis-oriented ZnO NRs using the sonicated sol–gel immersion method, on the ZnO seed-layer obtained by spin coating especially on glass substrate presented in this paper, has rarely been reported. These grown ZnO nanorods exhibit the PPC effect in which photoconductivity persists even after terminating the UV illumination [29]. Other nanostructured materials such as monolayer MoS$_2$ flakes, nanowires of GaN, thin films of CdS, and single crystals of SrTiO$_3$ [30–33] also have been found to exhibit the PPC effect. The PPC effect with extremely long decay time and a very slow recovery rate involves novel applications for holographic memories [33], bi-stable optical switches [34], and radiation detectors [35]. The origin of the PPC is not clearly understood, and there is no universally established theory to explain this phenomenon. Madel et al. [3] investigated the influence of oxygen and argon ambient on the PPC in ZnO nanowires and suggested the PPC is related to the oxygen adsorption and desorption processes on the surface. It is most widely accepted that the PPC is a surface-related effect rather than bulk-related [36] and originates from the ZnO nanostructures due to the presence of oxygen vacancies [29, 36]. Due to low growth temperature, the ZnO nanorods have lattice defects and surface defects which can be reduced by post-annealing treatment. Thus, stabilized ZnO NRs

possess enhanced crystalline and application qualities owing to decreased oxygen vacancy concentration, deep level defects, and surface defect recombination [37]. Proper heat treatment viz. annealing temperature and duration, substrate temperature, gas environment, etc., is an effective way to obtain high-quality ZnO material along with improved optical properties [38–40].

The present paper gives the systematic study of modification in (i) the structure and morphology of ZnO films, intended to be chosen as seed-layer, by varying one of the sol–gel-method process-parameter, (ii) the aspect ratio of vertically aligned ZnO NRs by changing seed-layer-molarity and immersion time and (iii) structural, morphological and other properties of ZnO film, i.e., seed-layer and ZnO NR arrays after annealing. We have used the low temperature sonicated-sol–gel-immersion method to grow the vertically aligned ZnO NRs on a coated glass substrate. The photoluminescence (PL) and photoconductivity studies are also performed which lead to interesting results.

2 Experimental

Vertically aligned, i.e., c-axis aligned ZnO NRs on ZnO-seed-layer have been grown and studied. Initially, a zinc oxide thin film is deposited on a glass substrate which acts as a seed-layer, and then ZnO NRs are grown over it. The method is described below.

2.1 Materials

Zinc acetate (99.99% pure) was purchased from Sigma-Aldrich. Isopropanol (99.80% pure), monoethanolamine (99.50% pure), and hexamethylenetetramine (99.50% pure) were purchased from Merck KGaA. Zinc nitrate hexahydrate (99.99% pure) was purchased from SD Fine Chemicals Limited. All the chemicals were used without further purification.

2.2 Deposition of seed-layer

ZnO seed-layer is prepared on a glass substrate using a sol–gel spin coating method. The precursor solution was prepared using a 0.05 M solution of zinc acetate [Zn(CH$_3$COO)$_2$] in isopropanol and monoethanolamine (MEA). The presence of MEA helps in

stabilizing the sol. The solution was magnetically stirred at 50 °C for 1 h and then aged for 24 h at room temperature 25 °C. The precursor solution thus obtained was spin coated on a duly cleaned glass substrate. The glass substrates were cleaned in an ultrasonic cleaner using methanol, acetone, and deionized water [41]. Spinning was done for 30 s at a speed of 2000 rpm. The film was then heated from room temperature to 200 °C, kept for 10 min and then allowed to cool back to room temperature. The process of spinning and heating was repeated ten times for obtaining appreciable thickness to facilitate crystalline structure. The final annealing of the film was done at 450 °C for three hours. Similarly, four more films were deposited with precursor solutions having molarity 0.1 M, 0.2 M, 0.4 M, and 0.6 M. The films are named as 0.05 M seed, 0.1 M seed, 0.2 seed, 0.4 M seed, and 0.6 M seed. Thus, prepared seed-layers were examined by XRD and those found suitable were used for the growth of ZnO NRs.

2.3 Growth of ZnO NRs

On the seed-layer-coated glass substrates, the ZnO NR arrays are grown using the sonicated sol–gel immersion method [16]. In this process, 0.1 M molar solutions of zinc nitrate hexahydrate [$Zn(NO_3)_2.6-H_2O$] and hexamethylenetetramine [HMT($C_6H_{12}N_4$)] were prepared separately in deionised water using magnetic stirring for 30 min. HMT works as a surfactant. In a conical flask, both the solutions were then mixed together and sonicated at 50 °C for 30 min using an ultrasonic water bath (Ultrasonic cleaner, LABMAN-40 kHz) following which it was magnetically stirred and aged for 3 h at room temperature. The resulting solution was poured into an autoclave bottle containing a seed-layer-coated glass substrate, in a slant position such that the coated surface faces the bottom. The autoclave bottle was capped tightly and immersed in a hot water bath maintained at 95 °C for 4 h after which the prepared sample was carefully taken out, washed with deionised water, and then dried in air. All the as-grown samples were noticeably stable and showed very good adherence to the substrate as it did not get disturbed during washing. Thus, ZnO NR arrays were grown on all seed-layer-coated glass substrates except 0.05 M seed-layer since crystallinity has not developed in it as inferred from the XRD pattern, Fig. 1a. These samples were named as 0.1Mseed/

NRs/4 h, 0.2Mseed/NRs/4 h, 0.4Mseed/NRs/4 h, and 0.6Mseed/NRs/4 h.

The structure and morphology of these samples were examined to select suitable seed-layer-molarity for the growth of ZnO NRs. As the molarity of the precursor solution for growing NRs on each seed-layer was kept constant at 0.1 M, the only variable besides seed-layer-molarity is immersion time. Accordingly, three additional samples of ZnO NRs were then grown for different immersion times, i.e., 1, 2, and 6 h for the selected seed-layer-molarity 0.1 M. Thus, now there are samples for four different immersion times named as 0.1Mseed/NRs/1 h, 0.1Mseed/NRs/2 h, 0.1Mseed/NRs/4 h, and 0.1 M seed/NRs/6 h.

To summarize, we have used five different molarities 0.05 M, 0.1 M, 0.2 M, 0.4 M, 0.6 M for seed-layers and four different immersion times 1 h, 2 h, 4 h, and 6 h for growing nanorods and grown total twelve samples. The 0.1 M molarity of the precursor solution was kept constant for every growth process of NRs. First, we have changed the seed-layer molarity and kept the immersion time 4 h. Next, we have varied the immersion time for the chosen seed-layer-molarity of 0.1 M.

Finally, the best sample chosen from the above samples on the basis of structural and morphological analysis was annealed at 400 °C for 2 h. The annealing temperature is kept lower than that for the seed-layer (450 °C) so that the seed-layer may not get affected.

2.4 Characterization

The structural study of the sample has been performed by X-Ray diffractometer (Model-Rigaku Ultima IV) to confirm the formation of ZnO, for 2θ values ranging from 20 to 90° using CuK$_\alpha$ radiation (λ = 1.540598 Å). The surface and cross-sectional morphology of the samples were observed using FESEM (Model-JEOL) to confirm the growth of NRs. The transmission and absorption spectra have been recorded using a UV–Vis spectrophotometer (Model-V670, Jasco), and the photoluminescence (PL) spectra have been obtained using a fluorescence spectrometer (Model LS-55, Perkin Elmer) for excitation wavelength 325 nm. The photoconductivity measurements, which include current–voltage characterstics and photoresponse, have been done by making electrical contacts using silver paste on the
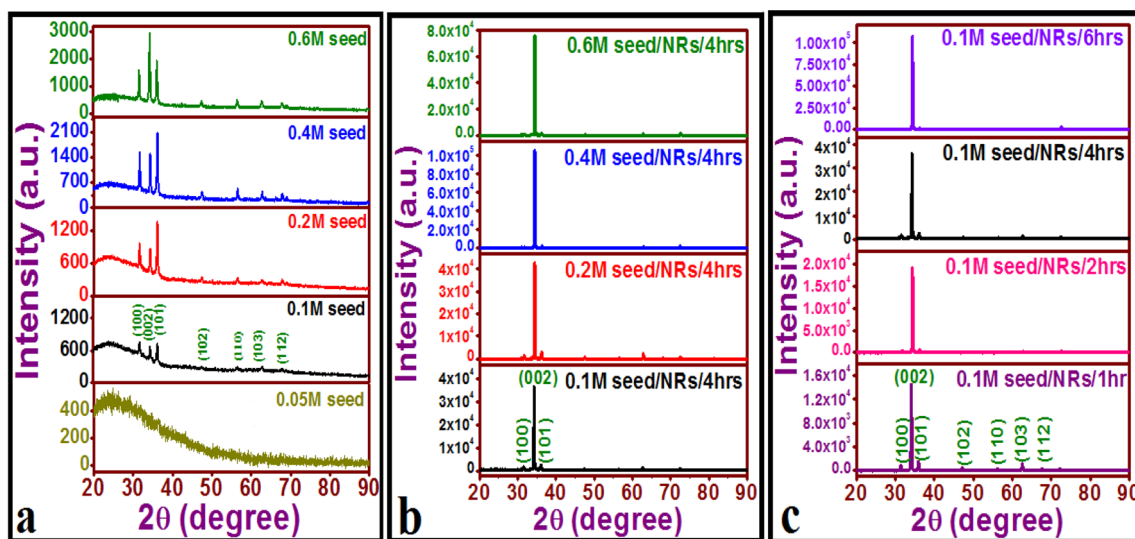
Fig. 1 XRD patterns of the **a** seed-layers corresponding to different molarities of the precursor solution, **b** NRs on different seed-layers for a fixed immersion time of 4 h, and **c** NRs grown for different immersion times on 0.1 M seed-layer

sample with an electrode spacing of 10 mm. The area of illumination was 1 cm^2, and the photo-excitation source was a 300 W UV lamp. The dark- and photo-current under UV illumination of 365 nm is recorded by a multimeter (RISH Multi-18S) with adapter RISH Multi SI-232. All these measurements have been done at room temperature.

3 Results and discussion

3.1 Influence of seed-layer-molarity and immersion time on ZnO NRs

The XRD patterns of the films deposited using precursor solutions of different molarities, i.e., 0.05, 0.1, 0.2, 0.4, and 0.6 M are shown in Fig. 1a. The film corresponds to 0.05 M molarity does not show crystalline nature and is therefore not selected for the seed-layer, here. The other four films show a polycrystalline nature. In these films, XRD peaks occur along (100), (002), (101), (102), (110), (103), and (112) planes, indicating hexagonal wurtzite structure of ZnO according to JCPDS Card No. 005-0664 and Refs. 16, 41. The major peaks are along (100), (002), and (101) planes. These four crystalline films are chosen as seed-layers for the growth of ZnO NRs the precursor solution of which is 0.1 M molar as mentioned earlier.

The corresponding four XRD patterns are shown in Fig. 1b. The highly intense (002) peak indicating

growth along the c-axis is obtained for 2θ values lying between 34.24° and 34.44° which confirms the hexagonal wurtzite structure of ZnO for the NRs. The crystallite-size t_{DS} along different crystallographic planes as calculated by well-known Scherrer equation [42] is given as

$$t_{DS} = \frac{0.9\lambda}{\beta COS\theta} \qquad (1)$$

where t_{DS} is crystallite size, λ is the x-ray wavelength and β is the full width at half maximum (FWHM) of the x-ray peak on the 2θ axis in radians. In the seed-layer, the crystallite-size increases from 5 to 10 nm and in NRs it increases from 48 to 53 nm with an increase in the seed-layer-molarity are given in Table 1.

The top view of the FESEM images, Fig. 2a–c, of the seed-layers, shows uniformly distributed grains of average size 29, 34, and 40 nm for seed-layers corresponding to 0.1 M, 0.4 M, and 0.6 M, respectively. Inset of Fig. 2c shows the high magnification image at × 700,000 of 0.6 M seed-layer and reveals that seed-layer is constituted of small nano-sized grains having a size less than 5 nm. The SEM of the cross section of the 0.1 M seed-layer has been obtained, Fig. 2d, to facilitate comparison with that of nanorods.

The surface morphologies of ZnO NRs grown on seed-layers of molarity 0.1, 0.2, 0.4, and 0.6 M are shown in Fig. 3a–c, and d, respectively. It can be seen that the rise in the grain size of seed-layers, which

Table 1 Results from the structural and morphological study of the ZnO samples. S.No.6 is shown again at S.No.12 for quick comparison

S.No	Sample	Structural and morphological evaluation					
0.05–0.6 M Seed-layer							
	Seed-layers	Crystallite size (nm) from XRD along			Average grain size from FESEM (nm)		
		(100)	(002)	(101)			
1	0.05 M seed	Amorphous					
2	0.1 M seed	5.81	7.29	6.18	29		
3	0.2 M seed	6.35	6.30	9.14	–		
4	0.4 M seed	8.11	8.86	9.99	34		
5	0.6 M seed	7.97	10.25	9.98	40		
0.1–0.6 M Seed-layer/NRs/1-6 h							
	Grown NRs	Crystallite size (nm)	XRD Intensity	Mean diameter D (nm)	Standard deviation σ	Length L (nm)	Aspect ratio (L/D)
6	0.1 M seed/NRs/4 h	48.58	35,835	197.34	58.92	1650	8.38
7	0.2 M seed/NRs/4 h	53.54	42,709	293.26	76.38	1583	5.40
8	0.4 M seed/NRs/4 h	53.49	106,036	373.39	134.19	2585	6.93
9	0.6 M seed/NRs/4 h	53.39	75,687	138.95	51.26	1060	7.68
10	0.1 M seed/NRs/1 h	40.41	14,529	135.30	45.21	832	6.16
11	0.1 M seed/NRs/2 h	50.84	19,126	155.73	70.82	1500	9.68
12	0.1 M seed/NRs/4 h	48.58	35,835	197.34	58.92	1650	8.38
13	0.1 M seed/NRs/6 h	55.33	106,591	339.37	77.84	2446	7.22

acts as a nucleation site for the growth of NRs, causes an increment in the diameter D of the hexagonal NRs. The insets of Fig. 3a–d show the histogram of distribution in diameter of NRs and the standard deviation σ. Figure 3e–h show the cross-sectional view of the NRs. The diameter increases with molarity up to 0.4 M and beyond that, for 0.6 M it is found to decrease. The NRs grown on 0.6 M seed-layer do not have flat facets instead have upwards spiralling hexagonal facet indicating further growth of the NRs. The diameter D with standard deviation σ, length L, and aspect ratio (L/D) of the NRs is represented in Table 1. From the NRs grown on different seed-layers-molarities, the one which shows a high aspect ratio and the relatively low standard deviation is chosen for further study.

A large standard deviation indicates that the diameters of NRs are spread out over a wider range of values, while the smaller standard deviation indicates that the diameters tend to be close to the mean value. The NRs that have grown on 0.1 M seed-layer (Fig. 3a and e) show the maximum aspect ratio with small σ. Thus, the 0.1 M molarity for the seed-layer is chosen to optimize the growth of NRs with a narrow diameter and longer length by varying the immersion time duration.

The XRD patterns of four samples of ZnO NRs on 0.1 M molarity-seed-layers grown separately using 0.1 M molar precursor solution for different time durations of 1, 2 and 6 h are shown in Fig. 1c. NRs grown for 4 h immersion are reproduced here for ready comparison.

The surface morphology of these NRs is presented in Fig. 4a–c which shows a hexagonal cross section. With an increase in immersion time from one to six hours, the intensity of the (002) peak increases, Fig. 1c, indicating an increment in the length of the NRs. This inference conforms to the cross-sectional FESEM of the NRs showing their lengths, Figs. 3e and 4d–f. Table 1 (s.no.10–13) shows the variation of the (002) peak intensity and height of the NRs with respect to the immersion time. Both the diameter and length increase with increased immersion time. The 6-h-immersion provides the longest NRs, but the corresponding diameter is also very large. The standard deviation σ is least for 1-h-immersion-NRs, but the aspect ratio is also small. The 2-h-immersion gives maximum aspect ratio but corresponding σ is

Fig. 2 FESEM images of seed-layer with different molarities **a** 0.1 M, **b** 0.4 M, **c** 0.6 M and **d** cross-sectional image of 0.1 M seed-layer. Inset shows the FESEM image at high magnification (× 700,000)
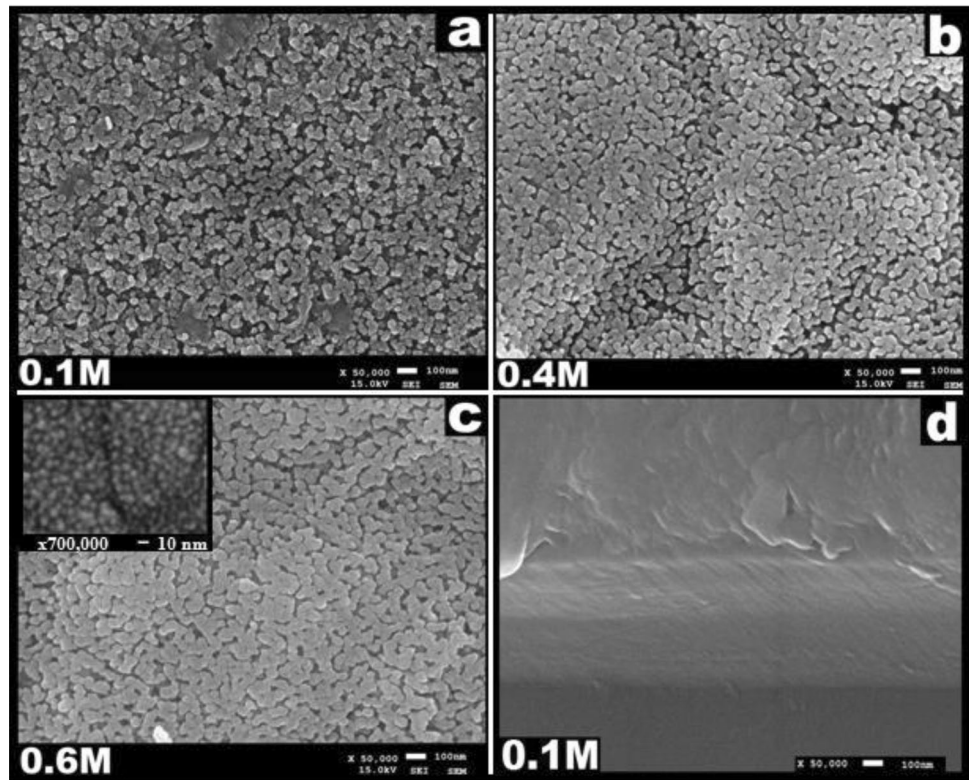
also high. The 4 h immersion offers a relatively high aspect ratio and small σ. So the 4 h immersion time is suitable for narrow and longer NRs with respect to high aspect ratio and low σ.

Based on the above results, ZnO NRs sample 0.1 M seed/NRs/4 h, i.e., 0.1 M precursors for seed-layer as well as NRs with 4 h immersion time has been selected for further study. The chosen sample is annealed at 400°C for 2 h.

3.2 Structural, morphological and other properties of the chosen seed-layer (0.1 M) and as-grown NRs (0.1 M seed/NRs/4 h); and annealed NRs (0.1 M seed/NRs/4 h)

In this section, structural, morphological, and other properties of the 0.1 M seed-layer, the chosen as-grown NRs (0.1 M seed/NRs/4 h), and thereafter annealed NRs are presented. The results are as follows.

3.2.1 Structural analysis

The XRD pattern of the chosen sample after annealing is shown in Fig. 5. The XRD patterns of the corresponding seed-layer and as-grown NRs are also reproduced here, from Fig. 1, for purpose of quick comparison. The as-grown and annealed NR samples show a sharp narrow peak along (002) centered at 34.24° and 34.30°, respectively, and the peaks along (100) and (101) are negligibly small as compared to that along (002).

In annealed NRs, these peaks are still smaller. The highly intense peak along (002) plane is indicating single-crystalline nature as well as the preferential growth of NRs along the c-axis, i.e., perpendicular to the substrate. The FWHM value is least for the (002) peak, Table 2. FWHM of all the peaks for as-grown NRs is lesser than those for seed-layer and decreases further after annealing the NRs. The noticeable decrease in the value of FWHM along the c-axis for annealed NRs indicates that annealing improves the crystalline quality of the nanorods. Narrowing of XRD peaks after annealing has been reported earlier also [4, 43]. Crystallite size along (002) plane increases monotonically after each step of synthesis and lies between 7 and 52 nm for seed-layer, as-grown, and annealed NRs, Table 2. Annealing induces coalescence of small grains by grain boundary diffusion [44] leading to the formation of larger crystallites.

Fig. 3 Top views (**a**–**d**) and a corresponding cross-sectional view of ZnO NRs grown on seed-layers of different molarities (**e**–**h**). The inset shows the histogram corresponding to the NRs diameter with standard deviation
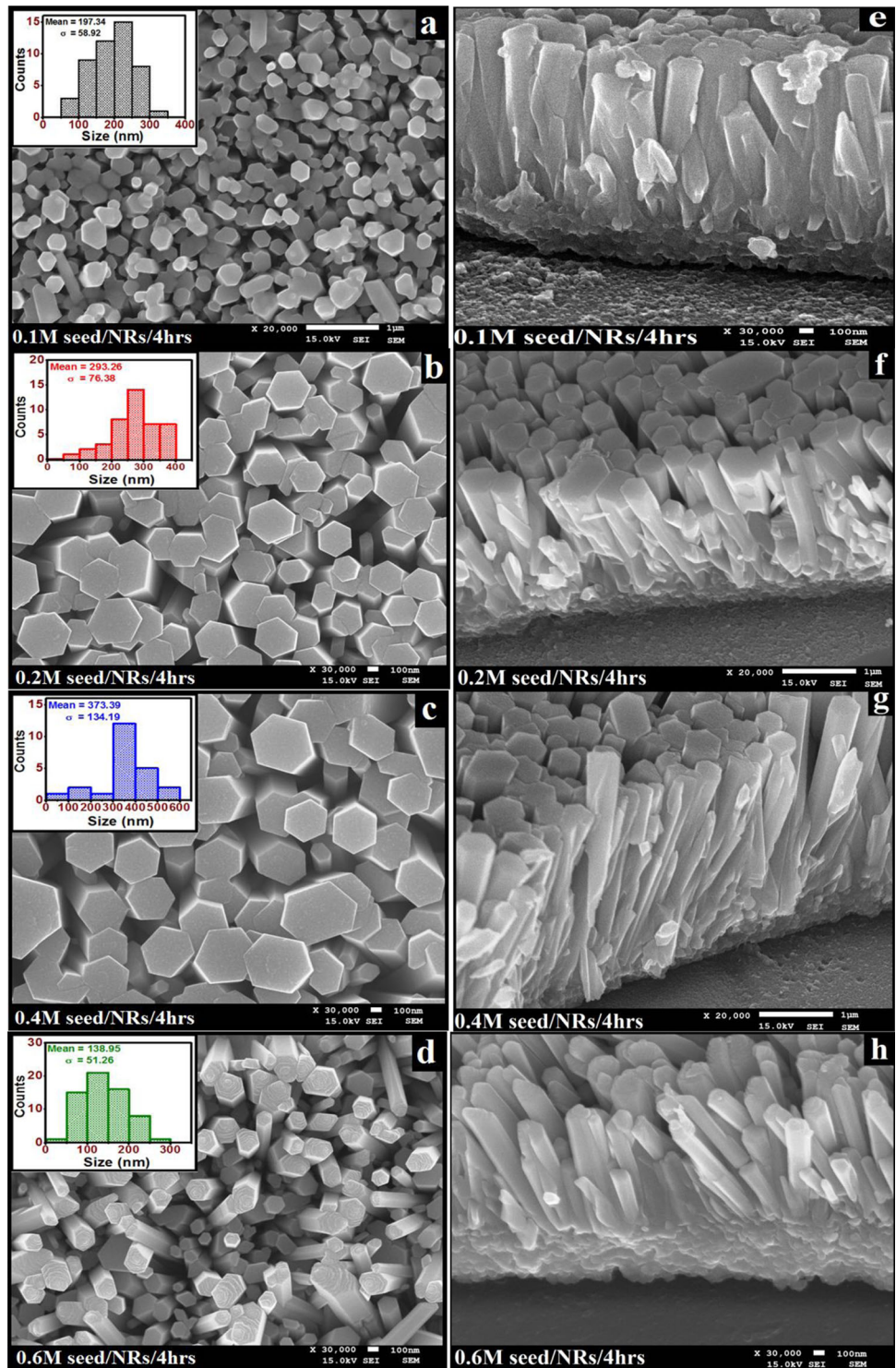

The dislocation density δ calculated using Williamson and Smallman's Equation [42]

$$\delta = \frac{1}{t_{DS}^2} \qquad (2)$$

is seen to reduce fast from 295×10^{14} to 3.74×10^{14} as the synthesis proceeds from seed-layer to as-grown NRs and then to annealed NRs.

The lattice constants 'a' and 'c' are determined using the equation given below [42]

Fig. 4 Top views (**a**–**c**) and a cross-sectional view (**d**–**f**) of ZnO NRs grown on 0.1 M seed-layer by varying the immersion time as 1, 2, and 6 h. The inset shows the histogram corresponding to the diameter of NRs with standard deviation
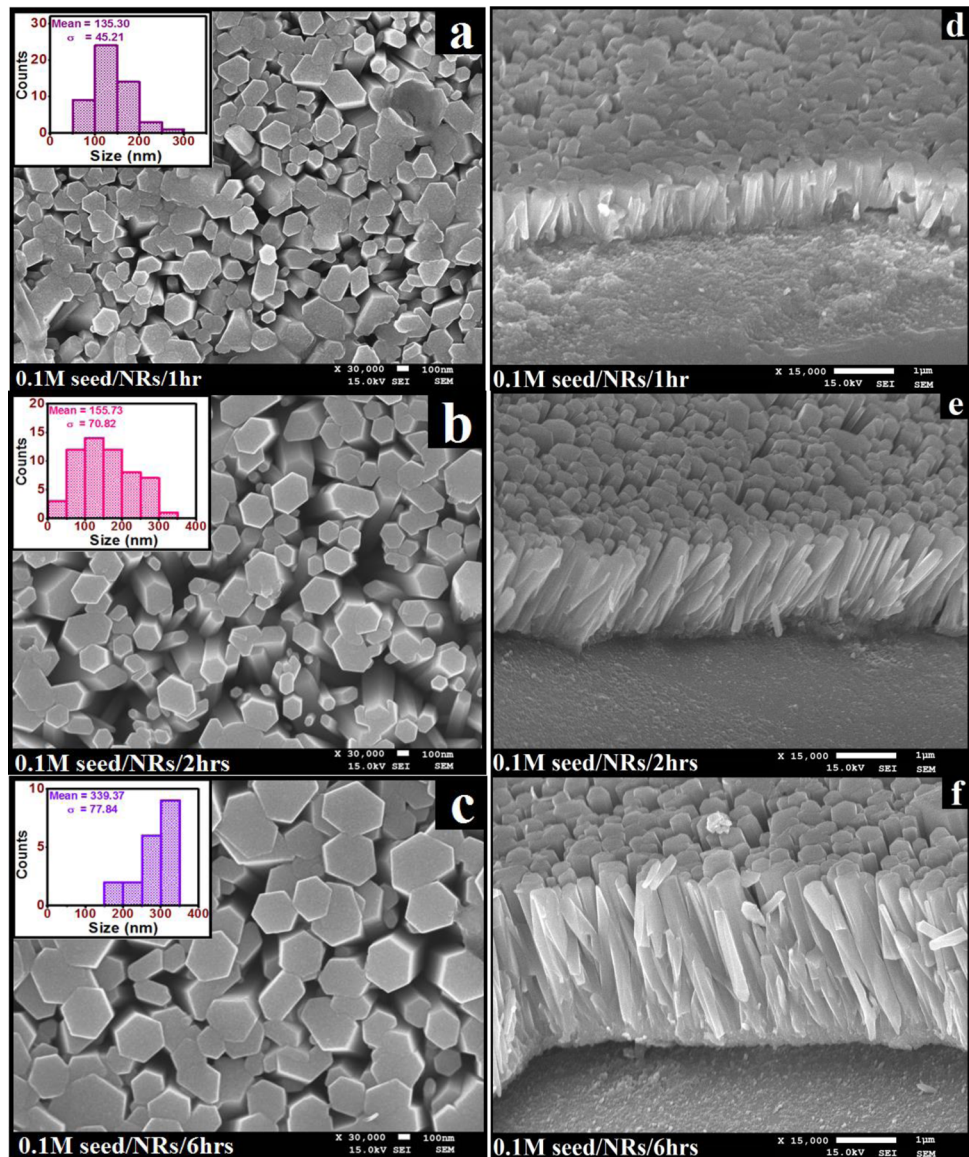
$$\frac{1}{d_{hkl}^2} = \frac{4}{3}\left[\frac{h^2 + hk + k^2}{a^2}\right] + \frac{l^2}{c^2} \tag{3}$$

along with Bragg's law. The lattice constant 'a' is found to be 3.260, 3.274 and 3.264 Å, and lattice constant 'c' is found to be 5.206, 5.236, and 5.227 Å for seed-layer as-grown NRs and annealed NRs, respectively. The lattice constants shrink after annealing but are larger for both the NRs than those for seed-layer as well as bulk ZnO for which a = 3.249 Å & c = 5.205 Å.

The strain ε_Z along the c-axis is determined by the equation

$$\varepsilon_z = \frac{(c - c_0)}{c_0} \tag{4}$$

where c is the lattice constant of the films calculated above and c_0 (= 5.205 Å) is the strain-free lattice constant for the ZnO powder and the biaxial film stress ($-453.6 \times 10^9 \varepsilon_z$) is proportional to c-axis strain [45]. All the samples have positive strain, i.e., tensile strain [46]. The strain and stress are less in seed-layer and high in as-grown NRs because of the growth of nanostructures, i.e., nanorods. The amount of strain and subsequently stress decreases after annealing the NRs which can be attributed to larger crystallite size leading to improvement in the crystalline quality of NRs as can also be seen by a higher intensity of the XRD peak, Table 2.
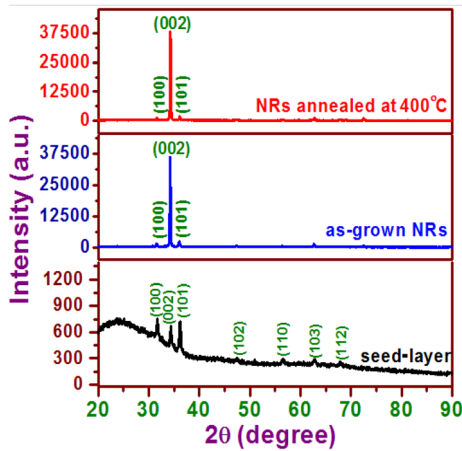
Fig. 5 XRD patterns of the seed-layer, as-grown, and annealed NRs for the sample named 0.1 M seed/NRs/4 h

3.2.2 Surface morphology

The FESEM images shown in Fig. 6a, c, and e reveal the surface morphology i) of the ZnO seed-layer on a glass substrate, ii) of ZnO NRs on the seed-layer, and iii) that of ZnO NRs after annealing, respectively. Also, the magnified images of the top view of ZnO NRs before and after annealing are shown in Fig. 6d and f, respectively. Figure 6b, g, and h shows the cross-sectional FESEM images of the seed-layer, as-grown, and annealed ZnO NRs, respectively.

Figure 6a–c and g has been reproduced from the figures in Sect. 3.1. The seed-layer shows uniformly distributed nano-sized grains.

At some places, grains have joined resulting in larger ones. The seed-layer thickness is estimated to be $\sim$ 545 nm from the cross-sectional view. Inset of Figs. 6c and e shows the histogram of the diameter-distribution of as-grown and annealed NRs and the standard deviation σ. Inset of Fig. 6d shows the top view of one of the nanorods with perfect hexagonal structure. Vertically aligned hexagonal-shaped NRs with flat-top facets and high areal density are observed on the entire surface of the seed-layer having a mean diameter of 197.34 nm with a standard deviation of 58.92 as per the histogram for as-grown NRs. The sharpness of these hexagonal-shaped NRs improves with shrinkage of diameter after annealing as shown in Figs. 6e and f. The diameter of the NRs reduces by 39% and their areal density increases. The FESEM image of the top facet of NRs shows some arc-like marks which turns into a spiralling structure after annealing (compare Fig. 6d and f).

The cross-sectional FESEM image of as-grown NRs shows that they are well aligned vertically on the seed-layered substrate. The cross-sectional FESEM image of as-grown NRs shows that they are well

Table 2 The FWHM, intensity, crystallite size, dislocation density, lattice constants, strain, and stress for the seed-layer, as-grown, and annealed NR samples

S. No	Sample		Seed-layer	As-grown NRs	NRs annealed at 400 °C
1	FWHM (degree)	(100)	1.42	0.238	0.195
		(002)	1.14	0.171	0.161
		(101)	1.35	0.266	0.251
2	Intensity	(100)	753	1208	1003
		(002)	490	35,835	37,890
		(101)	695	2030	1541
3	Crystallite size (nm)	(100)	5.81	34.68	42.40
		(002)	7.29	48.59	51.73
		(101)	6.18	31.38	33.27
4	Dislocation density δ (10^{14} lines/m^2)	(100)	295	8.31	5.56
		(002)	185	4.24	3.74
		(101)	261	10.16	9.03
5	Lattice constant	a (Å)	3.260	3.274	3.264
		c (Å)	5.206	5.236	5.227
		c/a	1.597	1.599	1.601
6	Strain ($\varepsilon_Z \times 10^{-3}$)		0.298	5.96	4.26
7	Stress ($\times 10^9$ Pa)		− 0.135	− 2.70	− 1.93

Fig. 6 Top & cross-sectional view of seed-layer (**a**, **b**), as-grown NRs (**c** and **g**) and annealed NRs (**e** and **h**) of the sample parameters '0.1 M seed/NRs/4 h'. (**d**) and (**f**) shows a high magnification view, at × 50,000, of as-grown and annealed NRs. Inset of both Figs. 6c and e shows the histogram of the diameter-distribution of NRs and the standard deviation. Inset of Fig. 6d shows the top view of one of the nanorods with perfect hexagonal structure
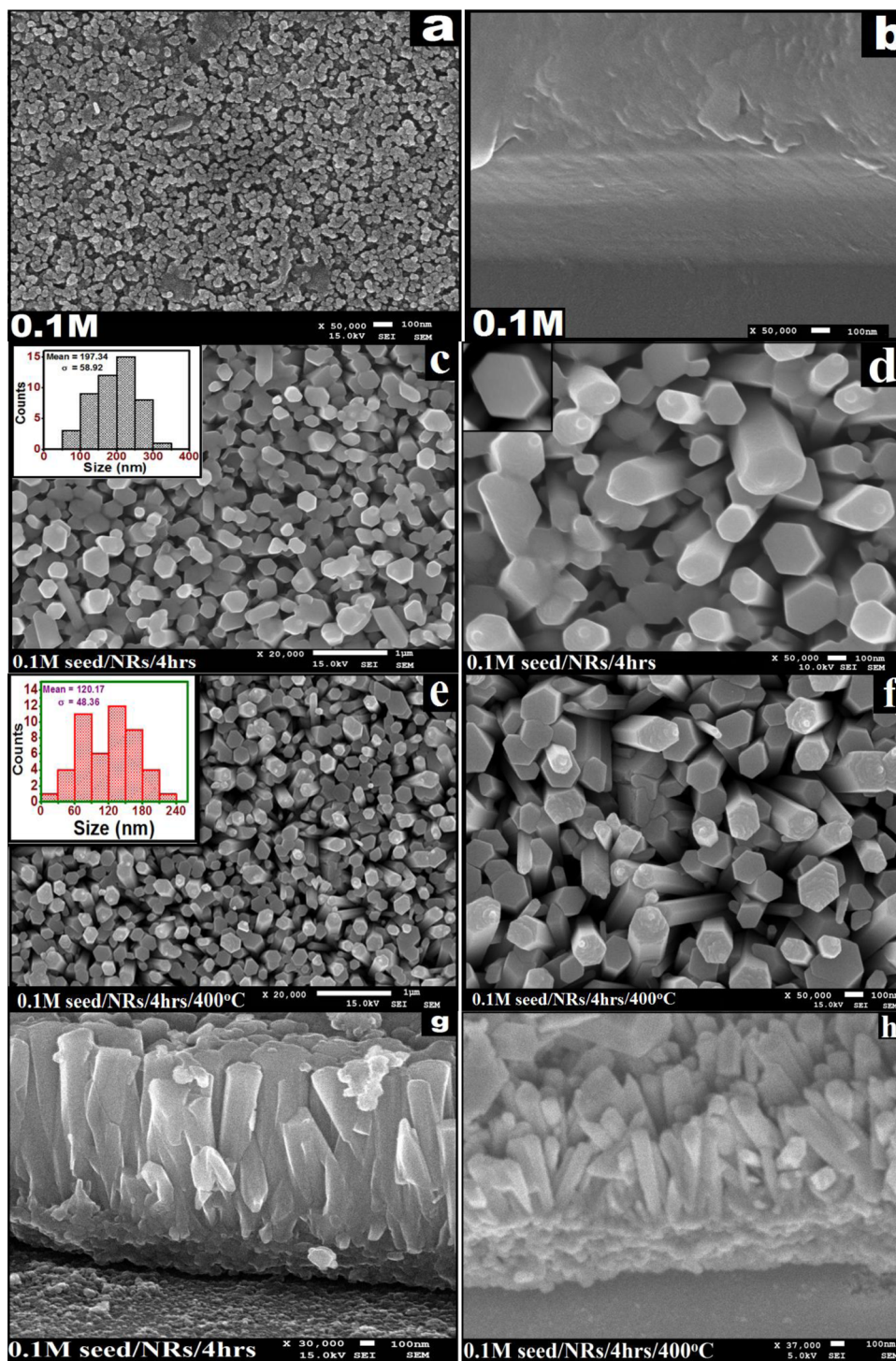
aligned vertically on the seed-layered substrate. Annealing disturbs this vertical alignment which may be attributed to the shrinkage of the NRs or the shrinkage of seed grains. The length of the as-grown NRs reduces after annealing from 1.6–1.7 to 0.65–0.70 μm. The morphology of NRs changes apparently with the annealing as the aspect ratio is found to decrease from 8.11 to 5.41. Such an effect of annealing on ZnO nanorods in powder form, i.e., not on any substrate and not vertical, grown by hydrothermal treatment has been reported by Zhang et al. [37].

The reduction in seed-layer thickness after the growth of NRs, Fig. 6g, confirms that the grains of the seed-layer provide a foundation for NRs to grow vertically in a well-aligned manner. Seed-layer used for growing NRs in different growth conditions has also been reported [9, 47]. ZnO NRs reported using different growth methods for seed-layers as well are summarized here in Table 3 for ready reference.

3.2.3 Optical studies and optical band gap

The transmittance T (Fig. 7a) and absorbance A (Fig. 7b) of the seed-layer, as-grown, and annealed NRs are recorded in the wavelength range 350–900 nm and are shown here. All the samples have transparency of less than 70% and show cut off below 400 nm. The seed-layer sample is more transparent, and its transparency decreases after the growth of ZnO NRs as a result of the change in the morphology of the film. The formation of highly c-axis-oriented ZnO NRs reduces the light transmission due to (i) increased thickness of the sample which includes the length of the NRs as well as (ii) light scattering due to array of NRs. The decrease in transmittance after the growth of ZnO NRs has been also reported previously [17, 19]. The annealing of the NRs improves the sample transparency slightly, which may be due to shrinkage in length as well as the diameter of ZnO NRs after annealing, as observed in the FESEM image mentioned in the preceding section. But the transparency is still much less than that for the seed-layer.

The absorption spectra of the three samples show high absorbance in the UV region (below 400 nm) and low absorbance in the visible region of the spectrum. The seed-layer sample shows the least absorbance, and as-grown NRs show the highest absorption in conformation to the transmission spectra. The absorption edges are around 390 nm, 392 nm and 396 nm for the seed-layer, as-grown, and annealed NRs, respectively. This monotonic red shift in the absorption may due to a monotonic increase in crystallite size from ~ 7 to ~ 52 nm presented in Table 2.

The optical band gap values are obtained by plotting $(\alpha h\nu)^2$ versus $h\nu$ graph, Tauc's plot, shown in the inset of Fig. 7b. Here, α is the absorption coefficient and $h\nu$ is the energy of photon incident on the sample. The optical band gap values are obtained by extrapolating the linear portion of the curve to intercept the energy axis. The band gap values are estimated to be 3.22, 3.21, and 3.18 eV for the seed-layer, as-grown and annealed NRs, respectively, and are found less as compared to that of bulk ZnO which is 3.37 eV. The band gap values of as-grown and annealed ZnO NRs decrease relative to that of the seed-layer by 10 meV and 40 meV, respectively. Hence, the band gap value of bulk ZnO can be tuned up to 190 meV by the growth of NRs as well as annealing of NRs. The band gap value decreases by 30 meV after annealing as compared to that for as-grown NRs, which may be due to increased crystallite size as found by XRD.

3.2.4 Photoluminescence

The PL emission spectra of all the prepared samples are recorded with an excitation wavelength of 325 nm and are shown in Fig. 8. The PL spectra exhibit UV emission at 397 nm (3.123 eV) for seed-layer and 404 nm (3.069 eV) for as-grown NRs as well as annealed NRs. In the visible region, the seed-layer exhibits two sharp peaks centered at 450 and 486 nm with a shoulder at 522 nm while as-grown and annealed samples show three sharp emission peaks centered at 450, 486, and 527 nm with a shoulder at 579 nm.

The near band edge (NBE)-related UV emission peak at 397 nm for the seed-layer has larger intensity than that of defect-related peaks in the visible region. The NBE emission originates from the radiative recombination of the free exciton-exciton collision process in ZnO [53] and shows a red shift of 54 meV after the growth of NRs. This red shift remains unaffected by annealing. The red shift of the NBE emission may be due to the interaction of the adsorbed oxygen atoms with neutral acceptors or due to tensile strain on the VBM [43].

Regarding visible emission, annealing results in a reduction in the intensity of the peaks at 486 nm and 527 nm. The blue emission peak at 450 nm and blue-green emission peak at 486 nm corresponding to the seed-layer show no shift, but shoulder in the green region at 522 nm reinvents into a sharp peak at 527 nm after the growth of NRs. The annealing of NRs although quenches the green emission partially but does not affect the peak position.

Earlier, red shifts in UV emission of ~ 30 and ~ 44 meV have been reported [43] due to annealing in air and oxygen, respectively, for hydrothermally

Table 3 Earlier reported ZnO NRs on seed-layer-coated substrates, in the literature

Substrate	ZnO Seed-layer deposition method	ZnO NRs growth method	Length (μm)	Diameter (nm)	Ref
FTO	Spin coating	solution-growth	0.6	60	[9]
p-type Si	RF sputtering	CBD	1.22	61.27	[10]
Glass	Sol–gel spin coating	CBD	0.3–2.0	30–120	[11]
Si (100)	RF sputtering	Thermal evaporation	5.5	1500	[12]
	PLD		2–4	80–250	
Quartz	RF sputtering	Hydrothermal	–	75–210	[13]
Glass	Sol–gel spin coating	Hydrothermal	0.24–1.2	57–230	[14]
Glass	Sol–gel spin coating	Hydrothermal	0.18–0.35	–	[15]
ITO	Sol–gel spin coating	Liquid Phase Epitaxy	1.0	40	[20]
ITO	Sol–gel spin coating	Solvothermal	–	106–336	[21]
ITO	Sol–gel spin coating	CBD	–	120–390	[22]
ITO	Sol–gel spin coating	Hydrothermal	2.9	66	[23]
Si (100)	PLD	Vapor–liquid-solid (VLS)	1.2	100–450	[24]
Si	Sol–gel spin coating	CBD	1.0	150	[25]
Si	Magnetron sputtering	Hydrothermal	–	96	[26]
Si (100)	Sol–gel spin coating	Aqueous-solution method	–	50–470	[27]
n-type Si(100)	ECR-PLD	Solution-based method	1.2- 2.2	150–219	[48]
p-type Si (100)	Sol–gel spin coating	Hydrothermal	–	20–50	[49]
p-type Si	Sol–gel spin coating	Hydrothermal	0.45–1.2	80–120	[50]
Soda-lime glass	Sol–gel spin coating	Hydrothermal	–	80–114	[51]
Nylon	RF sputtering	Hydrothermal	0.95	90	[52]

Fig. 7 Transmittance (**a**) and absorption (**b**) spectra of the ZnO-seed-layer and NR samples. Inset shows the Tauc plot
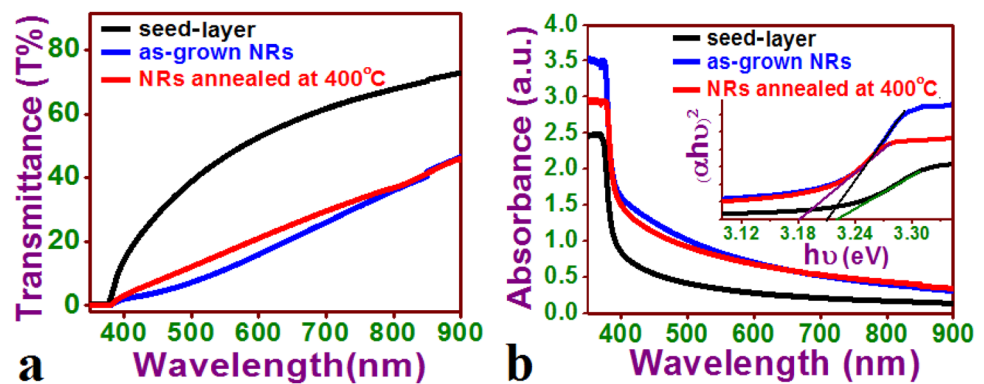
grown ZnO nanorods on the ZnO seed-layer deposited on a quartz substrate using RF magnetron sputtering. Other researchers have reported UV emissions at 400 nm from Al-doped ZnO nanodisks and nanorod clusters in powder form [54], at 405 nm from ZnO/graphene hybrids on Si substrate [55], and ∼ 410 nm from Li-doped ZnO NRs on ITO-coated substrate [56].

The origin of visible emission is attributed to the intrinsic defects such as oxygen vacancy (V_O), zinc vacancy (V_{Zn}), oxygen interstitial (O_i), zinc interstitial (Zn_i), oxygen anti-site (O_{Zn}), and zinc anti-site (Zn_O)

theoretically explained by Zhang et al. [57], Xu et al. [58], Janotti et al. [59] and Erhart et al. [60]. The donor (Zn_i, V_O, Zn_O) and acceptor (V_{Zn}, O_i, O_{Zn}) can exist in a neutral state or charged state, and their positions within the bandgap of ZnO have been reported in the literature by different groups [57–68]. These donor/acceptor energy levels within the band gap can generate a range of transitions with different energies which can be observed experimentally as PL emission from ZnO-based samples in UV or visible region of the electromagnetic spectrum. Refs. 61, 62, 63 report the position of the Zn_i level at 0.22 eV below
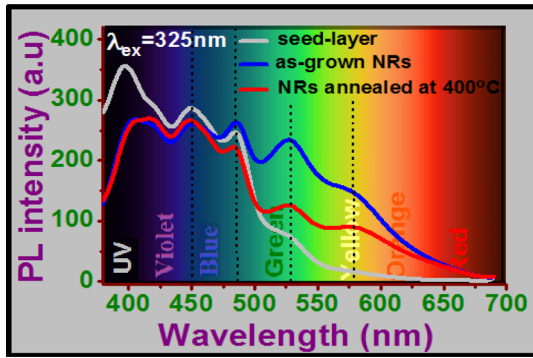
Fig. 8 Photoluminescence spectra of ZnO seed-layer, as-grown and annealed ZnO NRs

the conduction band minima (CBM) where the CBM is at 3.37 eV above the valence band maxima (VBM). Some authors have reported Zn_i to be 2.9 eV above VBM [58, 64–66]. Broadly speaking, there are multiple states of Zn_i which are located between 2.7 and 3.0 eV [67]. The position of V_O levels with their three charge states (V_O^0, V_O^+, and V_O^{++}) is not clear. The V_O^0, V_O^+ and V_O^{++} states are estimated to be located ∼ 0.6 eV [57, 60, 68], ∼ 1.0 eV [63, 65, 67, 68], and ∼ 2.0 eV [67, 68] below the CBM, respectively. The zinc antisites (Zn_O) owing to their very high formation energies are quite improbable [59]. The V_{Zn} level is located at 0.3 eV above the VBM [58, 60–66]. The O_i levels may be located anywhere between 0.4 eV [58, 60, 62–65] and 1.09 eV [63] above the VBM. The O_{Zn} levels are located at 1.0 eV and 1.5 eV above the VBM [58, 61, 62, 64]. Based on these mentioned energy levels, the possible PL emissions from ZnO-based samples are represented schematically in Fig. 9 in colors corresponding to their emission energy. Also, these transitions are summarized in Table 4.

Based on this, the visible-emissions occurring in our experiment are correlated as: (i) the blue emission at 450 nm (2.76 eV) is due to the transition $Zn_i \rightarrow VB$ (2.7–3.0 eV), (ii) the blue-green emission at 486 nm (2.55 eV) is due to the transition $Zn_i \rightarrow V_{Zn}$ (2.4–2.7 eV), (iii) the green emission at 527 nm (2.35 eV) is caused by the transition $V_O^+ \rightarrow VB$ (2.40 eV) and (iv) the yellow shoulder emission at 579 nm (2.14 eV) is related to the transition $V_O^+ \rightarrow V_{Zn}$ (2.10 eV).

The reduction in NBE emission for as-grown and annealed NRs can be attributed to the increment in surface-related defects. The growth of vertically aligned NRs offers a higher surface-to-volume ratio and thereby facilitates a larger number of oxygen

vacancies, as they are more likely to form on the surface, which results in the increased green emission. The PL intensity of green emission, for annealed NRs, gets quenched up to large extent and can be associated with a reduction in the concentration of oxygen vacancies due to annealing in air. Successive reductions in green emission after annealing in air and in oxygen have been reported earlier [43].

3.2.5 Photoconductivity studies

3.2.5.1 I-V characteristics The I-V characteristics for the three samples in question, in dark and under UV illumination, plotted on a log–log scale, are shown in Fig. 10 for a voltage application between 0 and 30 V. The variations of dark current I_{dc}, Fig. 10a and the photocurrent I_{pc}, Fig. 10b with applied voltage for seed-layer, as-grown and annealed NRs follow the power-law relationship, $I \propto V^r$, where r is the slope of individual straight portion segments. $r < 1$ shows sub-linear, $r = 1$ shows linear, i.e., ohmic behavior and r > 1 shows super-linear behavior of current with voltage [69, 70].

The dark current, as well as photo-current variation with voltage for the seed-layer, changes its nature at the point V = 7 V on log scale below which shows sublinear behavior. Above 7 V, the variation is superlinear. For as-grown NRs, the dark and photocurrents both follow close to linear variation with $r = 1.05$ and 1.02, respectively. For annealed NRs, the dark current variation with the voltage shows linear behavior with $r = 1.00$, and photocurrent shows
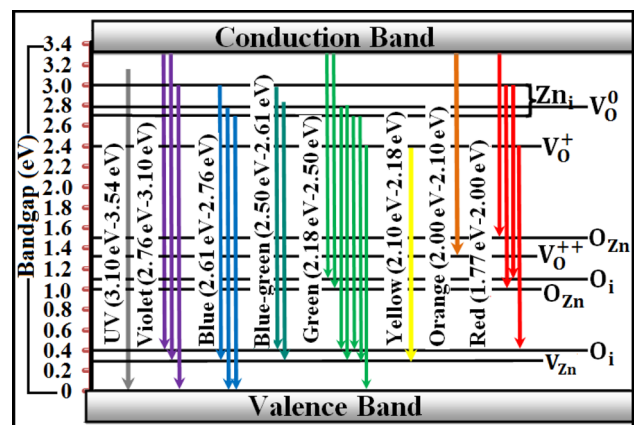

Fig. 9 Schematic of the radiative transitions possible in ZnO-based samples estimated on the basis of energy levels suggested by various authors referred here. The colors correspond to the emission line

Table 4 The radiative transitions possible in ZnO-based samples

PL emission	Possible transitions
UV (350 nm–400 nm)	Near band-edge (NBE)
Violet (400 nm–450 nm)	$\mathbf{Zn_i}$→VB; CB → $\mathbf{O_i}$; CB → $\mathbf{V_{Zn}}$
Blue (450 nm–475 nm)	$\mathbf{V_O^0}$→VB; $\mathbf{Zn_i}$→VB; $\mathbf{Zn_i}$→$\mathbf{V_{Zn}}$
Blue-green (475 nm–495 nm)	$\mathbf{Zn_i}$→$\mathbf{O_i}$ or $\mathbf{Zn_i}$→$\mathbf{V_{Zn}}$
Green (495 nm–570 nm)	CB→$\mathbf{O_i}$ or CB→ $\mathbf{O_{Zn}}$ or $\mathbf{V_O^0}$→$\mathbf{O_i}$ or $\mathbf{V_O^0}$ →$\mathbf{V_{Zn}}$ or $\mathbf{Zn_i}$ → $\mathbf{O_i}$ or $\mathbf{Zn_i}$ → $\mathbf{V_{Zn}}$ or $\mathbf{V_O^+}$→VB
Yellow (570 nm–590 nm)	$\mathbf{V_O^+}$→$\mathbf{V_{Zn}}$
Orange (590 nm–620 nm)	CB → $\mathbf{V_O^{++}}$
Red (620 nm–700 nm)	CB → $\mathbf{O_{Zn}}$ or $\mathbf{Zn_i}$ → $\mathbf{O_{Zn}}$ or $\mathbf{Zn_i}$ → $\mathbf{O_i}$ or $\mathbf{V_O^+}$→$\mathbf{O_i}$

super linear behavior with $r = 1.23$, Fig. 10 and Table 5.

The sub-linear behavior indicates the flow of trap-limited current, whereas the super-linear behavior relates to the flow of space-charge-limited current (SCLC) inside the material. The SCLC results when excess carriers are injected from one of the electrodes [70–72]. The adsorption and desorption of chemisorbed oxygen molecules on the sample surface modify the SCLC. Such modification is strong when the surface to volume ratio is high as in the present structures, i.e., nanorods. The concentration of injected-free-carriers can exceed that of free-carriers in the sample as chemisorptions of oxygen depletes free electrons thereby enhancing SCLC. The injected electrons can be taken up by physisorbed oxygen molecules to get chemisorbed. Besides this, traps existing in the sample also modify the SCLC because of which r can rise beyond a value of 2 which is not happening here.

3.2.5.2 Photoresponse The photoresponse of the samples can be studied in terms of the time-resolved rise and decay photocurrent spectrum of the samples

as shown in Fig. 11. The measurement is performed using 365 nm UV light for illumination of the samples at a bias voltage of 5 V for 5 min OFF, 30 min ON, and again for OFF condition. Under OFF condition, very small dark current appears in case of seed-layer which is many times larger for as-grown NRs. Upon exposure to UV light, the photocurrent rapidly increases for initial five minutes after which it becomes saturated and remains as such as long as the UV illumination is ON. There is no decay of photocurrent under UV illumination for all the samples. As UV illumination is turned off, the photocurrent from the seed-layer falls rapidly, then decreases slowly with time and finally becomes constant at a value little higher than the initial dark current, in several minutes, Fig. 11a. For NRs—as-grown and annealed—the photocurrent follows very slow decay. It falls only about 7% for as-grown and 30% for annealed NRs after 30 min of UV termination, Fig. 11b.

The dark and photocurrent values for seed-layer, as-grown, and annealed NRs are represented in Table 5. For the seed-layer, the magnitude of the dark current is 0.008 μA. It is 0.620 μA for as-grown NRs

Fig. 10 Variation of **a** dark current I_{dc} and **b** photocurrent I_{pc} as a function of applied voltage for seed-layer, as-grown and annealed ZnO NRs samples
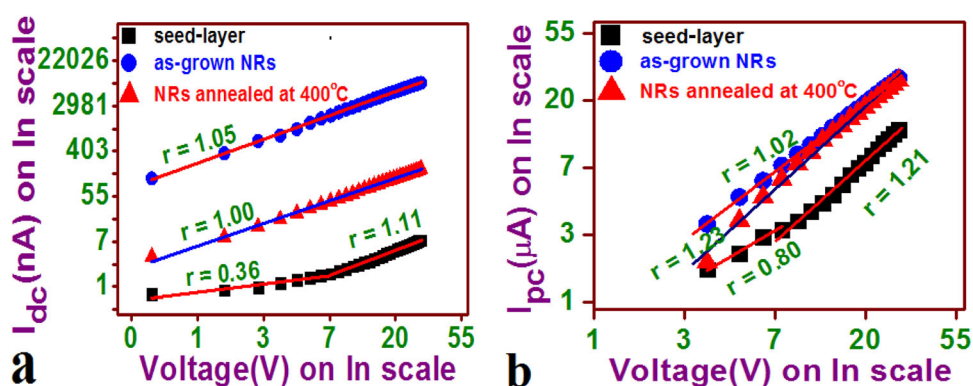
Table 5 Slopes for the variation of the dark- and photo-currents (I_{dc} and I_{pc}) with variation in applied voltage corresponding to Fig. 10, the maximum value of I_{dc} and I_{pc} in the time-resolved study, and rise time of the photocurrent for the seed-layer, as-grown and annealed NR samples corresponding to Fig. 11

Sample	Slopes for dark current (I_{dc})	Slopes for Photo current (I_{pc})	Total current ($I_{dc} + I_{pc}$) (μA)	Maximum dark current I_{dc} (μA)	Maximum photo current I_{pc} (μA)	Rise time τ_r (sec)
Seed-layer	r1 = 0.36 r2 = 1.11	r1 = 0.80 r2 = 1.21	3.76	0.008	3.752	56
As-grown NRs	r = 1.05	r = 1.02	4.84	0.620	4.220	78
NRs annealed at 400 °C	r = 1.00	r = 1.23	4.55	0.021	4.529	161

and 0.021 μA for annealed NRs. The value of photocurrent increases from 3.752 to 4.529 μA from seed-layer to as-grown NRs to annealed NRs. Even though I_{pc} for annealed NRs is larger compared to that for as-grown NRs, the total current ($I_{dc} + I_{pc}$) comes out to be lesser because of much reduced dark current.

The process of adsorption and desorption of oxygen molecules on the surface of the ZnO NRs causes the dark current as well as photocurrent. In the adsorption process, the oxygen molecules of the atmosphere close to the sample surface capture the free electrons from the n-type ZnO and generate oxygen ions which create a depletion layer near the surface resulting in low conductivity in dark. In the desorption process, the adsorbed oxygen ions trap the photogenerated holes and produce oxygen molecules which reduces the depletion layer resulting in a high photocurrent under UV illumination. After terminating the UV illumination, the fast decay is attributed to rapid change in the density of charge carrier, and the slow decay is described by trapping and de-trapping of charge carrier at trap states.

The enhancement in photocurrent after growth of NRs on the seeded substrate is related to the higher surface-to-volume ratio which provides a large surface area to generate more electron–hole pairs, under UV illumination, for oxygen desorption thereby increasing the density of charge carriers. Further enhancement in I_{pc} after annealing in air, Table 5, could be associated with the drop in oxygen vacancies thereby reducing the trap centers for photogenerated carriers [73]. This can also be related to the PL spectra where the observed reduction in the green emission is the evidence of lessening of the oxygen vacancies after annealing the NRs in air. Thus, the reduction in oxygen vacancies reduces the trapping of photogenerated electrons resulting in increased photocurrent.

The rise time τ_r during which photocurrent rises from 20 to 80% of its peak value is estimated to be 56, 78, and 161 s for seed-layer, as-grown, and annealed NRs, respectively. The decay portion of the photo-response curve, Fig. 11a, for the seed-layer is quite sharp and well fitted with bi-exponential equation $I = I_0 + I_1 \exp(-t/\tau_{d1}) + I_2 \exp(-t/\tau_{d2})$. The two relaxation time constants τ_{d1} and τ_{d2} are estimated to be 64 s and 549 s, respectively.

The decay of I_{pc} for as-grown and annealed NRs is very slow as well as very small even after 7 h of cessation of UV. It is shown for duration of more than seven hours in Fig. 12 which also includes the information of Fig. 11b. This phenomenon of slow decay over a long time, i.e., over several hours to several days after terminating the UV illumination is termed as persistent photoconductivity (PPC). PPC is much large for as-grown NRs as compared to that for annealed ones. Bao et al. [74] investigated the persistent photoconductivity in ZnO nanowires in air and vacuum conditions and found that the PPC is much larger in a vacuum than in air.

The mechanism of PPC is associated with oxygen vacancies (V_O) with three charge states—V_O, V_O^+ and V_O^{++}. The V_O is a stable neutral state; singly ionized (V_O^+) and doubly ionized (V_O^{++}) vacancies are metastable charged states [75, 76]. The different lattice relaxation involved with the charged states causes an energy barrier which prevents the immediate change of metastable state into the stable neutral state. Eventual decay of the singly ionized state into the neutral state requires a long time interval but does not require ambient oxygen [76]. These metastable states act as trap states and play a crucial

Fig. 11 Photoresponse, i.e., time-resolved rise and decay photocurrent spectrum of **a** seed-layer and **b** as-grown as well as annealed NRs of ZnO
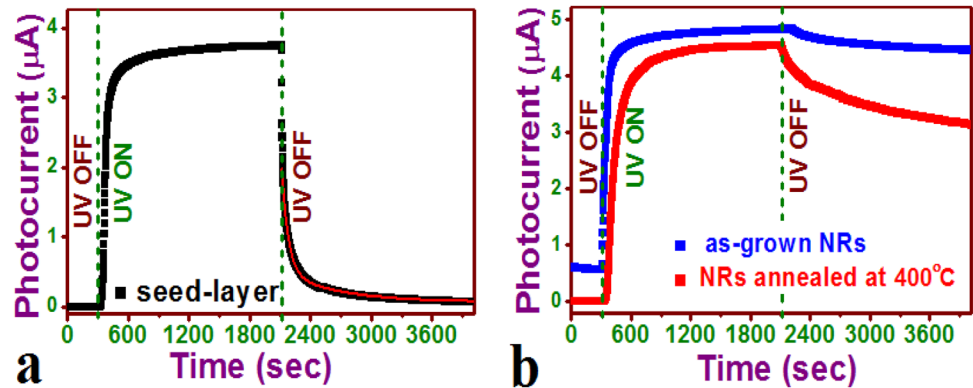

role in the generation and recombination of the photo-generated electron.

Under the UV illumination, plenty of photo-generated electrons can be excited in the conduction band according to the following equations:

(i)   direct band-to-band transition:

$$ZnO + h\nu \rightarrow e^- + h^+ \tag{5}$$

(ii)   photo-ionization of oxygen vacancies into its metastable states, as shown in Fig. 13a:

$$V_O + h\nu \rightarrow V_O^+ + e^- \text{ or } V_O^{++} + 2e^- \tag{6a}$$

$$V_O^+ + h\nu \rightarrow V_O^{++} + e^- \tag{6b}$$
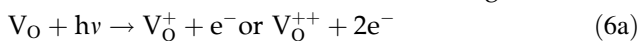
(iii)   indirect band-to-band transition involves two steps:

(a)   trapping of photoexcited electrons in metastable states:

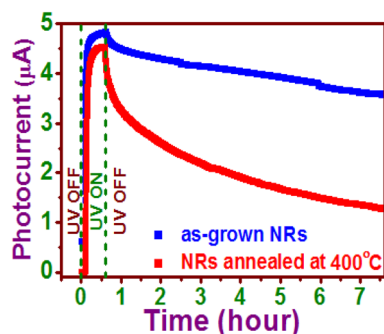**Fig. 12** The behavior of the persistent photoconductivity in as-grown and annealed NRs for 7 h of UV termination

$$V_O^{++} + 2e^- \rightarrow V_O \tag{7a}$$

$$V_O^{++} + e^- \rightarrow V_O^+ \tag{7b}$$

$$V_O^+ + e^- \rightarrow V_O \tag{7c}$$

(b)   photo-generation of electrons according to eqs. 6a & 6b

As the UV illumination is terminated, the photo-generated electrons present in the conduction band recombine with photo-generated holes in the valence band through direct band-to-band recombination and/or indirect recombination involving two steps which are the trapping of electrons from the conduction band in the metastable states according to Eqs. 7a, b and c, as shown in Fig. 13b and de-trapping of electrons from the metastable states for recombination as shown in Fig. 13c.

After cessation of the UV illumination, the trapping of photo-generated electrons from the conduction band reduces their number thereby reducing the oxygen re-adsorption process thereby preventing the widening of the depletion region, finally resulting in the transportation of photo-generated electrons which contribute to PPC. The large decay time is attributed to indirect recombination through trapping/de-trapping of electrons. The trapping of an electron from the conduction band in a metastable state significantly reduces the recombination rate and annihilates the direct recombination.

The trapped electrons are released back which slowly recombines with the hole, increasing the recombination lifetime and thereby giving rise to PPC. As the green emission is related to the oxygen vacancies our PL results strongly support this oxygen vacancy mechanism of PPC. When the UV

Fig. 13 Proposed mechanism of long decay time regarding ZnO NRs: **a** photoionization of oxygen vacancies V_o during UV illumination, **b** trapping of an electron by ionized V_o after terminating UV illumination and **c** indirect recombination of electron–hole via trap-states
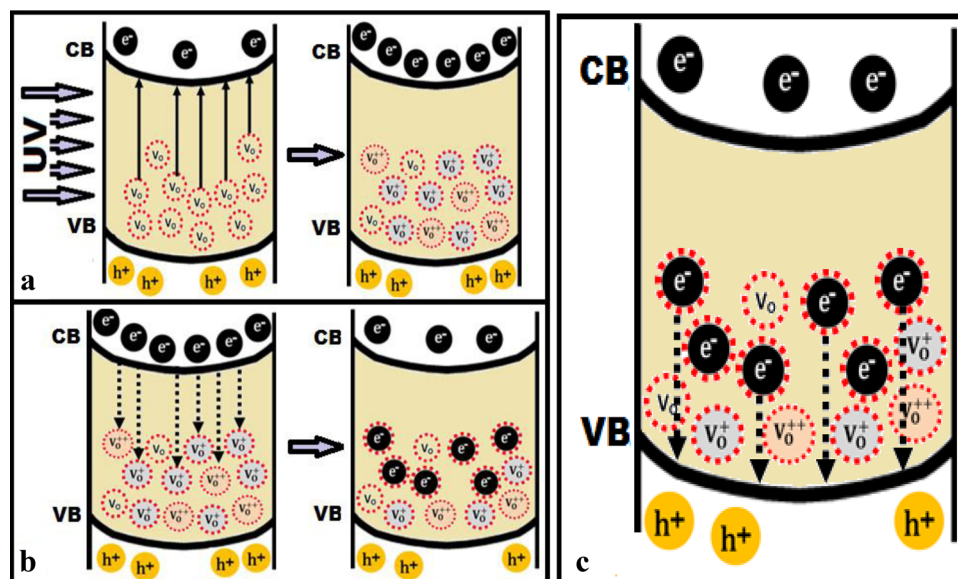
illumination is terminated, the oxygen vacancy deficient seed-layer exhibits rapid decay of photocurrent, i.e., no PPC while the as-grown and annealed NRs with the presence of large oxygen vacancies exhibit very slow decay of photocurrent, i.e., PPC. After 7 h of UV termination, the photocurrent falls only about 25% for as-grown and 72% for annealed NRs. The reduction in PPC of annealed NRs is due to the reduction in oxygen vacancies after annealing in air. Reyes et al. [77] reported the reduction in PPC by reducing oxygen vacancies through plasma treatment of the ZnO channels. Wang et al. [78] investigated the optical modulation of the ZnO NWs device and found IR radiation significantly shortened the decay time of the PPC.

4 Conclusion

Appropriate seed-layer of ZnO thin film with nano-sized grains has been deposited by spin coating on a glass substrate for the growth of NRs. On the seed-layer, highly c-axis-oriented vertically aligned hexagonal ZnO NRs with flat-top facets are grown by a low temperature sonicated-sol–gel-immersion method. The diameter and length of the NRs shrink after annealing. The band gap value decreases monotonically from the seed-layer to as-grown to annealed NRs and can be tuned by 190 meV as compared to bulk ZnO. The green emission from NRs quenches after air annealing which has been attributed to reduced oxygen vacancies. The ZnO NRs

exhibit persistent photoconductivity (PPC) with very slow decay due to the abundance of oxygen vacancies which act as a trap states for charge carrier to reduce the recombination rate. After seven hours of UV termination, the photocurrent falls only about 25% for as-grown and 72% for annealed NRs. After annealing the NRs, reduction in the oxygen vacancies partially suppresses the PPC. The observed persistent photoconductivity in grown ZnO NRs has a potential application in radiation detectors.

Acknowledgements

Compliance with ethical standards

Conflict of interest The authors declare that they have no conflict interest.

References

1. Z.L. Wang, Nanostructures of zinc oxide. Mater. Today **7**, 26–33 (2004)

2. A. Umar, C. Ribeiro, A. Al-Hajry, Y. Masuda, Y.B. Hahn, Growth of highly c-axis-oriented ZnO nanorods on ZnO/glass substrate: growth mechanism, structural, and optical properties. J. Phys. Chem. C **113**, 14715–14720 (2009)

3. M. Madel, F. Huber, R. Mueller, B. Amann, M. Dickel, Y. Xie, K. Thonke, Persistent photoconductivity in ZnO nanowires: Influence of oxygen and argon ambient. J. Appl. Phys **121**, 124301 (2017)

4. B. Mondal, L. Dutta, C. Roychaudhury, D. Mohanta, N. Mukherjee, H. Saha, Effect of annealing temperature on the morphology and sensitivity of the zinc oxide nanorods-based methane senor. Acta Metall. Sin. (Engl. Lett.) **27**, 593–600 (2014)

5. P.S. Kumar, A.D. Raj, D. Mangalaraj, D. Nataraj, Hydrophobic ZnO nanostructured thin films on glass substrate by simple successive ionic layer absorption and reaction (SILAR) method. Thin Solid Films **518**, e183–e186 (2010)

6. P.S. Kumar, A.D. Raj, D. Mangalaraj, D. Nataraj, N. Ponpandian, L. Li, G. Chabrol, Growth of hierarchical based ZnO micro/nanostructured films and their tunable wettability behavior Appl. Surf. Sci. **257**, 6678–6686 (2011)

7. P.S. Kumar, P. Paik, A.D. Raj, D. Mangalaraj, D. Nataraj, A. Gedanken, S. Ramakrishna, Biodegradability study and pH influence on growth and orientation of ZnO nanorods via aqueous solution process. Appl. Surf. Sci. **258**, 6765–6771 (2012)

8. A. Georgea , A.D. Raja, A.A. Irudayaraj, D.M.A. Raj, J. Arumugam, S. J. Sundaram, J. Kennedy, K. Kaviyarasu, Influence of solvent and precursor concentration on the properties of NiV_2O_6 nanoparticles, Surf. Interfaces **21**, 100711 (2020).

9. D.-Y. Son, K.-H. Bae, H.-S. Kim, N.-G. Park, Effects of seed-layer on growth of ZnO nanorod and performance of perovskite solar cell. J. Phys. Chem. C **119**, 10321–10328 (2015)

10. P.F. Azad, N. Naderi, M.J. Eshraghi, A. Massoudi, The effect of seed-layer on optical and structural characteristics of ZnO nanorod arrays deposited by CBD method. J Mater Sci: Mater Electron **28**, 15495–15499 (2017)

11. A. Bramantyo, N.R. Poespawati, M. Kenji, Optimization of ZnO seed-layer for growth of vertically aligned ZnO nanorods on glass surface. JAP Conf. Proc. **4**, 011103 (2016)

12. H. Wang, Z.P. Zhang, X.N. Wang, Q. Mo, Y. Wang, J.H. Zhu, H.B. Wang, F.J. Yang, Y. Jiang, Selective growth of vertical-aligned ZnO nanorod arrays on Si substrate by catalyst-free thermal evaporation. Nanoscale Res. Lett. **3**, 309–314 (2008)

13. M. Babikier, D. Wang, J. Wang, Q. Li, J. Sun, Y. Yan, Q. Yu, S. Jiao, Cu-doped ZnO nanorod arrays: the effects of copper precursor and concentration. Nanoscale Res. Lett. **9**, 199 (2014)

14. A.H. Kurda, Y.M. Hassan, N.M. Ahmed, Controlling diameter, length and characterization of ZnO nanorods by simple hydrothermal method for solar cells. World J. Nanosci Eng. **5**, 34–40 (2015)

15. A. Pimente, S.H. Ferreira, D. Nunes, T. Calmeiro, R. Martins, E. Fortunato, Microwave synthesized ZnO nanorod arrays for UV sensors: a seed-layer annealing temperature study. Materials **9**, 299 (2016)

16. M.H. Mamat, Z. Khusaimi, M.Z. Musa, M.Z. Sahdan, M. Rusop, Novel synthesis of aligned Zinc oxide nanorods on a glass substrate by sonicated sol–gel immersion. Mater. Lett. **64**, 1211–1214 (2010)

17. D. Mudusu, K.R. Nandanapalli, S.R. Dugasani, S.H. Park, C.W. Tu, Zinc oxide nanorods shielded with an ultrathin nickel layer: tailoring of physical properties. Sci. Rep. **6**, 28561 (2016)

18. R. Nandi, D. Singh, P. Joshi, R.S. Srinivasa, S.S. Major, Effect of Ga-doped ZnO seed-layer thickness on the morphology and optical properties of ZnO nanorods. AIP Conf. Proc. **1512**, 410–411 (2013)

19. I. Saurdi, M.H. Mamat, M.F. Malek, M. Rusop, Preparation of aligned ZnO nanorod arrays on Sn-doped ZnO thin films by sonicated sol-gel immersion fabricated for dye-sensitized solar cell. Adv. Mater. Sci. Eng. **2014**, 636725 (2014)

20. Y.T. Yin, W.X. Que, C.H. Kam, ZnO nanorods on ZnO seed-layer derived by sol-gel process. J. Sol-Gel Sci. Technol. **53**, 605–612 (2010)

21. L.-X. Du, Y. Jiao, S.-Y. Niu, H. Miao, H.-B. Yao, K.-G. Wang, X.-Y. Hu, H.-B. Fan, Control of morphologies and properties of zinc oxide nanorod arrays by slightly adjusting their seed-layers. Nanomater. Nanotechno. **6**, 1–8 (2016)

22. A. Sholehah, A.H. Yuwono, The effects of annealing temperature and seed-layer on the growth of ZnO nanorods in a chemical bath deposition process. Int. J. Technol. **4**, 565–572 (2015)

23. W.-Y. Chang, C.-A. Lin, J.-H. He, T.-B. Wu, Resistive switching behaviors of ZnO nanorod layers. Appl. Phys. Lett. **96**, 242109 (2010)

24. J. Jie, G. Wang, Y. Chen, X. Han, Q. Wang, B. Xu, J.G. Hou, Synthesis and optical properties of well-aligned ZnO nanorod array on an undoped ZnO film. Appl. Phys. Lett. **86**, 031909 (2005)

25. E.G. Barbagiovanni, V. Strano, G. Franzò, I. Crupi, S. Mirabella, Photoluminescence transient study of surface defects in ZnO nanorods grown by chemical bath deposition. Appl. Phys. Lett. **106**, 093108 (2015).

26. X. Xu, C. Xu, Y. Lin, T. Ding, S. Fang, Z. Shi, W. Xia, J. Hu, Surface photoluminescence and magnetism in hydrothermally grown undoped ZnO nanorod arrays. Appl. Phys. Lett. **100**, 172401 (2012)

27. Z.N. Urgessa, O.S. Oluwafemi, E.J. Olivier, J.H. Neethling, J.R. Botha, Synthesis of well-aligned ZnO nanorods on silicon substrate at lower temperature. J. Alloys Compd. **580**, 120–124 (2013)

28. N.K. Reddya, M. Devika, C.W. Tu, Vertically aligned ZnO nanorods on flexible substrates for multifunctional device applications: Easy and cost-effective route. Mater. Lett. **120**, 62–64 (2014)

29. J. Nayak, J. Kasuya, A. Watanabe, S. Nozaki, Persistent photoconductivity in ZnO nanorods deposited on electro-deposited seed-layers of ZnO. J. Phys. Condens. Matter. **20**, 195222 (2008)

30. Y.-C. Wu, C.-H. Liu, S.-Y. Chen, F.-Y. Shih, P.-H. Ho, C.W. Chen, C.-T. Liang, W.-H. Wang, Extrinsic origin of persistent photoconductivity in monolayer MoS$_2$ field effect transistors. Sci. Rep. **5**, 11472 (2015)

31. R. Calarco, M. Marso, T. Richter, A.I. Aykanat, R. Meijers, A.V.D. Hart, T. Stoica, H. Luth, Size-dependent photoconductivity in MBE-Grown GaN−Nanowires. Nano Lett. **5**, 981–984 (2005)

32. H. Yin, A. Akey, R. Jaramillo, Large and persistent photoconductivity due to hole-hole correlation in CdS. Phys. Rev. Mater. **2**, 084602 (2018)

33. V.M. Poole, S.J. Jokela, M.D. McCluskey, Using persistent photoconductivity to write a low-resistance path in SrTiO$_3$. Sci. Rep. **7**, 6659 (2017)

34. T. Tanabe, M. Notomi, S. Mitsugi, A. Shinya, E. Kuramochi, Fast bistable all-optical switch and memory on a silicon photonic crystal on-chip. Opt. Lett. **30**, 2575–2577 (2005)

35. S.L. Nguyen, C.D. Malliakas, J.A. Peters, Z. Liu, J. Im, L.-D. Zhao, M. Sebastian, H. Jin, H. Li, S. Johnsen, B.W. Wessels, A.J. Freeman, M.G. Kanatzidis, Photoconductivity in TI$_6$SI$_4$: a novel semiconductor for hard radiation detection. Chem. Mater. **25**, 2868–2877 (2013)

36. Z.G. Yin, X.W. Zhang, Z. Fu, X.L. Yang, J.L. Wu, G.S. Wu, L. Gong, P.K. Chu, Persistent photoconductivity in ZnO nanostructures induced by surface oxygen vacancy. Phys. Status Solidi RRL **6**, 117–119 (2012)

37. J.-J. Zhang, E.-J. Guo, L.-P. Wang, H.-Y. Yue, G.-J. Cao, L. Song, Effect of annealing treatment on morphologies and gas sensing properties of ZnO nanorods. Trans. Nonferrous Met. Soc. China **24**, 736–742 (2014)

38. K.C. Dubey, A. Srivastava, A. Srivastava, R.K. Shukla, Oxygen pressure and heat treatment effect on nanocrystalline ZnO films grown by pulsed laser deposition. Optoelectron. Adv. Mat. Rapid Commun. **4**, 169–173 (2010)

39. R.K. Shukla, A. Srivastava, A. Srivastava, K.C. Dubey, Growth of transparent conducting nanocrystalline Al doped ZnO thin films by pulsed laser deposition. J. Cryst. Growth **294**, 427–431 (2006)

40. F. Zahedi, R.S. Dariani, S.M. Rozati, Effect of substrate temperature on the properties of ZnO thin films prepared by spray pyrolysis. Mater. Sci. Semicond. Process. **16**, 245–249 (2013)

41. A. Srivastava, N. Kumar, K.P. Misra, S. Khare, Enhancement of Band Gap of ZnO Nanocrystalline Films at a Faster Rate Using Sr Dopant. Electron. Mater. Lett. **10**, 703–711 (2014)

42. A. Srivastava, N. Kumar, S. Khare, Enhancement in UV emission and band gap by Fe doping in ZnO thin films. Opto-Electron. Rev. **22**, 68–76 (2014)

43. M. Babikier, J. Wang, D. Wang, Q. Li, J. Sun, Y. Yan, W. Wang, Q. Yu, S. Jiao, S. Gao, H. Li, Effect of annealing on lattice strain and near-band-edge emission of ZnO nanorods. Electron. Mater. Lett. **10**, 749–752 (2014)

44. D.-R. Hang, S.E. Islam, K.H. Sharma, S.-W. Kuo, C.-Z. Zhang, J.-J. Wang, Annealing effects on the optical and morphological properties of ZnO nanorods on AZO substrate by using aqueous solution method at low temperature. Nanoscale Res. Lett. **9**, 632 (2014)

45. M.K. Puchert, P.Y. Timbrell, R.N. Lamb, Post deposition annealing of radio frequency magnetron sputtered ZnO films. J. Vac. Sci. Technol. A **14**, 2220 (1996)

46. S.H. Park, T. Hanada, D.C. Oh, T. Minegishi, H. Goto, G. Fujimoto, J.S. Park, I.H. Im, J.H. Chang, M.W. Cho, T.Y. Inaba, Lattice relaxation mechanism of ZnO thin films grown on substrates by plasma-assisted molecular-beam epitaxy. Appl. Phys. Lett. **91**, 231904 (2007)

47. H. Seo, Y. Wang, G. Uchida, K. Kamataki, N. Itagaki, K. Koga, M. Shiratani, Growth control of ZnO nano-rod with various seeds and photovoltaic application. J. Phys.: Conf. Ser. **441**, 012029 (2013)

48. Z. Yu, H. Li, Y. Qiu, X. Yang, W. Zhang, N. Xu, J. Sun, J. Wu, Size-controllable growth of ZnO nanorods on Si substrate. Superlattices Microstruct. **101**, 469–479 (2017)

49. K.L. Foo, U. Hashim, K. Muhammad, C.H. Voon, Sol–gel synthesized zinc oxide nanorods and their structural and optical investigation for optoelectronic application. Nanoscale Res. Lett. **9**, 429 (2014)

50. Y.S. Bae, D.C. Kim, C.H. Ahn, J.H. Kim, H.K. Cho, Growth of ZnO nanorod arrays by hydrothermal method using homo-seed-layers annealed at various temperatures. Surf. Interface Anal. **42**, 978–982 (2010)

51. B. Santoshkumar, A. Biswas, S. Kalyanaraman, R. Thangavel, G. Udayabhanu, G. Annadurai, S. Velumani, Influence of defect luminescence and structural modification on the electrical properties of Magnesium Doped Zinc Oxide Nanorods. Superlattices Microstruct. **106**, 58–66 (2017)

52. S.M. Mohammad, Z. Hassan, R.A. Talib, N.M. Ahmed, M.A. Al-Azawi, N.M. Abd-Alghafour, C.W. Chin, N.H. Al-Hardan, Fabrication of a highly flexible low-cost H2 gas sensor

using ZnO nanorods grown on an ultra-thin nylon substrate. J Mater Sci: Mater Electron. **27**, 9461–9469 (2016)

53. A.S.H. Hameed, C. Karthikeyan, A.P. Ahamed, N. Thajuddin, N.S. Alharbi, S.A. Alharbi, G. Ravi, In vitro antibacterial activity of ZnO and Nd doped ZnO nanoparticles against ESBL producing Escherichia coli and Klebsiella pneumonia. Sci. Rep. **6**, 24312 (2016)

54. X. Qu, D. Jia, Controlled growth and optical properties of Al3+ doped ZnO nanodisks and nanorod clusters. Mater. Lett. **63**, 412–414 (2009)

55. J. Ding, X. Yan, Q. Xue, Study on field emission and photoluminescence properties of ZnO/graphene hybrids grown on Si substrates. Mater. Chem. Phys **133**, 405–409 (2012)

56. P. Ruankham, T. Sagawa, H. Sakaguchi, S. Yoshikawa, Vertically aligned ZnO nanorods doped with lithium for polymer solar cells: defect related photovoltaic properties. J. Mater. Chem. **21**, 9710–9715 (2011)

57. S.B. Zhang, S.-H. Wei, A. Zunger, Intrinsic n-type versus p-type doping asymmetry and the defect physics of ZnO. Phys. Rev. B **63**, 075205 (2001)

58. P.S. Xu, Y.M. Sun, C.S. Shi, F.Q. Xu, H.B. Pan, The electronic structure and spectral properties of ZnO and its defects. Nucl. Instr. Meth. Phys. Res. B **199**, 286–290 (2003)

59. A. Janotti, C.G. Van de Walle, Native point defects in ZnO. Phys. Rev. B **76**, 165202 (2007)

60. P. Erhart, K. Albe, A. Klein, First-principles study of intrinsic point defects in ZnO: Role of band structure, volume relaxation, and finite-size effects. Phys. Rev. B **73**, 205203 (2006)

61. C.H. Ahn, Y.Y. Kim, D.C. Kim, S.K. Mohanta, H.K. Cho, A comparative analysis of deep level emission in ZnO layers deposited by various methods. J. Appl. Phys. **105**, 013502 (2009)

62. R. Das, A. Kumar, Y. Kumar, S. Sen, P.M. Shirage, Effect of growth temperature on the optical properties of ZnO nanostructure grown by simple hydrothermal method. RSC Adv. **5**, 60365–60372 (2015)

63. S. Vempati, J. Mitra, P. Dawson, One-step synthesis of ZnO nanosheets: a blue-white fluorophore. Nanoscale Res. Lett. **7**, 470 (2012)

64. D. Behera, B.S. Acharya, Nano-star formation in Al-doped ZnO thin film deposited by dip-dry method and its characterization using atomic force microscopy, electron probe microscopy, photoluminescence and laser Raman spectroscopy. J. Lumin. **128**, 1577–1586 (2008)

65. M.J. Chithra, M. Sathya, K. Pushpanathan, Effect of pH on Crystal Size and Photoluminescence Property of ZnO Nanoparticles Prepared by Chemical Precipitation Method. Acta Metall. Sin. (Engl. Lett.) **28**, 394–404 (2015)

66. B. Lin, Z. Fu, Y. Jia, Green luminescent center in undoped zinc oxide films deposited on silicon substrates. Appl. Phys. Lett. **79**, 943–945 (2001)

67. K. Bandopadhyay, J. Mitra, Zn interstitials and O vacancies responsible for n-type ZnO: what do the emission spectra reveal? RSC Adv. **5**, 23540–23547 (2015)

68. Z.-M. Liao, H.-Z. Zhang, Y.-B. Zhou, J. Xu, J.-M. Zhang, D.-P. Yu, Surface effects on photoluminescence of single ZnO nanowires. Phys. Lett. A **372**, 4505–4509 (2008)

69. N. Kumar, A. Srivastava, Faster photoresponse, enhanced photosensitivity and photoluminescence in nanocrystalline ZnO films suitably doped by Cd. J. Alloys Compd. **706**, 438–446 (2017)

70. N. Kumar, A. Srivastava, Green photoluminescence and photoconductivity from screen-printed Mg doped ZnO films. J. Alloys Compd. **735**, 312–318 (2018)

71. R.W. Smith, A. Rose, Space-Charge-Limited Currents in Single Crystals of Cadmium Sulfide. Phys. Rev. **97**, 1531–1537 (1955)

72. A. Rose, An outline of some photoconductive processes. RCA Rev. **12**, 362–414 (1951)

73. S. Dhara, P.K. Giri, Enhanced UV photosensitivity from rapid thermal annealed vertically aligned ZnO nanowires. Nanoscale Res. Lett. **6**, 504 (2011)

74. J. Bao, I. Shalish, Z. Su, R. Gurwitz, F. Capasso, X. Wang, Z. Ren, Photoinduced oxygen release and persistent photoconductivity in ZnO nanowires. Nanoscale Res. Lett. **6**, 404 (2011)

75. S. Lee, A. Nathan, S. Jeon, J. Robertson, Oxygen defect-induced metastability in oxide semiconductors probed by gate pulse spectroscopy. Sci. Rep. **5**, 14902–14911 (2015)

76. R. Gurwitz, R. Cohen, I. Shalish, Interaction of light with the ZnO surface: Photon induced oxygen "breathing", oxygen vacancies, persistent photoconductivity and persistent photovoltage. J. Appl. Phys. **115**, 033701 (2014)

77. P.I. Reyes, C.-J. Ku, Z. Duan, Y. Xu, E. Garfunkel, Y. Lu, Reduction of persistent photoconductivity in ZnO thin film transistor-based UV photodetector. Appl. Phys. Lett. **101**, 031118 (2012)

78. Y. Wang, Z. Liao, G. She, L. Mu, D. Chen, W. Shi, Optical modulation of persistent photoconductivity in ZnO nanowires. Appl. Phys. Lett. **98**, 203108 (2011)